Journal of Solid State Chemistry **166,** 292–304 (2002)
doi:10.1006/jssc.2002.9589

Electronic, Magnetic, and Magnetoresistance Properties of the $n=2$ Ruddlesden–Popper Phases $Sr_3Fe_{2-x}Co_xO_{7-\delta}$ ($0.25 \le x \le 1.75$)

Gabriel M. Veith,* Rongji Chen,* Guerman Popov,* Mark Croft,† Yuliya Shokh,* Israel Nowik,‡ and Martha Greenblatt*,[1]

*Department of Chemistry and Chemical Biology, Rutgers, The State University of New Jersey, Piscataway, New Jersey 08854; †Department of Physics and Astronomy, Rutgers, The State University of New Jersey, Piscataway, New Jersey 08854; ‡Racah Institute of Physics, The Hebrew University, Jerusalem 91904 Israel

Received December 12, 2001; in revised form March 4, 2002; accepted March 15, 2002

A series of oxygen-deficient $n=2$ Ruddlesden–Popper phases, $Sr_3Fe_{2-x}Co_xO_{7-\delta}$ ($0.25 \le x \le 1.75$), were prepared by solid-state reactions. Temperature-dependent susceptibility and field-dependent magnetization data indicate that for $x \ge 0.25$ the dominant magnetic interactions are ferromagnetic. The onset of strong ferromagnetic interactions is evident at ~ 200 K, and a transition to a cluster-glass state is observed for all compositions below ~ 45 K. The temperature variation of resistivity for all the compounds shows variable-range hopping behavior with two different localization energy scales: one for $T < 40$ K and another for $T > 80$ K. Large negative magnetoresistance (the largest MR $\sim -65\%$ for $x = 0.25$) is observed for all phases. The magnetic susceptibility, Mössbauer and X-ray absorption near-edge spectroscopy data indicate that the formal oxidation state of Fe is close to 4+. The key role of d delocalization in the $Sr_3Fe_{2-x}Co_xO_{7-\delta}$ system is compared to the $Sr_3Fe_{2-x}Mn_xO_{7-\delta}$ series, where d localization dominates the properties.

1. INTRODUCTION

In the past 10 years there has been a great deal of interest in compounds which exhibit large magnetoresistance (MR), such as the perovskite manganites $Ln_{1-x}A_xMnO_3$ (Ln = trivanent cation, A = divalent cation) (1). In these materials, a large MR [$MR = (\rho_H - \rho_0)/\rho_0$, where ρ_H and ρ_0 are the resistivities at applied magnetic fields of H and 0, respectively] is manifested by a dramatic decrease in electrical resistance upon the application of a large magnetic field (2). Materials with large MR have a variety of potential applications including sensors and read-heads for computer hard-drives (2). The perovskite manganites exhibit large MR only in high magnetic fields, $H > 1$ T, and often below room temperature (1). Moreover, the occurrence of MR in the manganites involves a finely tuned balance between Mn^{3+}–O–Mn^{4+} double-exchange (DE), electron-phonon, and electron–electron interactions. The fundamental factors including the competition between metallic ferromagnetic (FM) and insulating paramagnetic and charge-ordered (CO) antiferromagnetic (AF) states controlling the MR effect are not completely understood. Therefore, the search for new materials with improved properties, appropriate for commercial applications, as well as a better understanding and concomitant control of the phenomena associated with MR continues.

The discovery of large MR in the layered perovskites, especially in the $n=2$ member of the $(La,Sr)_{n+1}Mn_nO_{3n+1}$ Ruddlesden–Popper (RP) series ($n = 1, 2, 3, \ldots, \infty$) (2, 3) has attracted considerable attention (4, 5). The structure of RP phases $[AO(ABO_3)_n]$ is made up of n perovskite blocks (ABO_3), separated by a rock salt AO layer as shown in Fig. 1 for the $n=2$ member. Alteration of insulating rock salt AO layers with conducting perovskite-like layers results in a two-dimensional (2D) character. In the quasi-low-dimensional (LD) RP systems, electronic correlations are enhanced and the magnetotransport behavior is expected to be interesting due to anisotropic transport and magnetic exchange interactions. Indeed, as mentioned above the $n=2$ RP phase $La_{1.8}Sr_{1.2}Mn_2O_7$ exhibits MR at much smaller applied magnetic fields than the corresponding isoelectronic three-dimensional (3D, $La_{0.6}Sr_{0.4}MnO_3$) manganite (3).

Similar to the manganites, cobalt-based perovskites are of great current interest. Recently, it was demonstrated that $SrFe_{1-x}Co_xO_3$ ($0.4 \le x \le 0.9$) is metallic and ferromagnetic above 300 K (6) and exhibits large negative MR (7). Similarly, Co substitution into the $n=2$ RP phases

[1] To whom correspondence should be addressed. Fax: (908) 445-5312. E-mail: greenblatt@rutchem.rutgers.edu.

0022-4596/02 $35.00

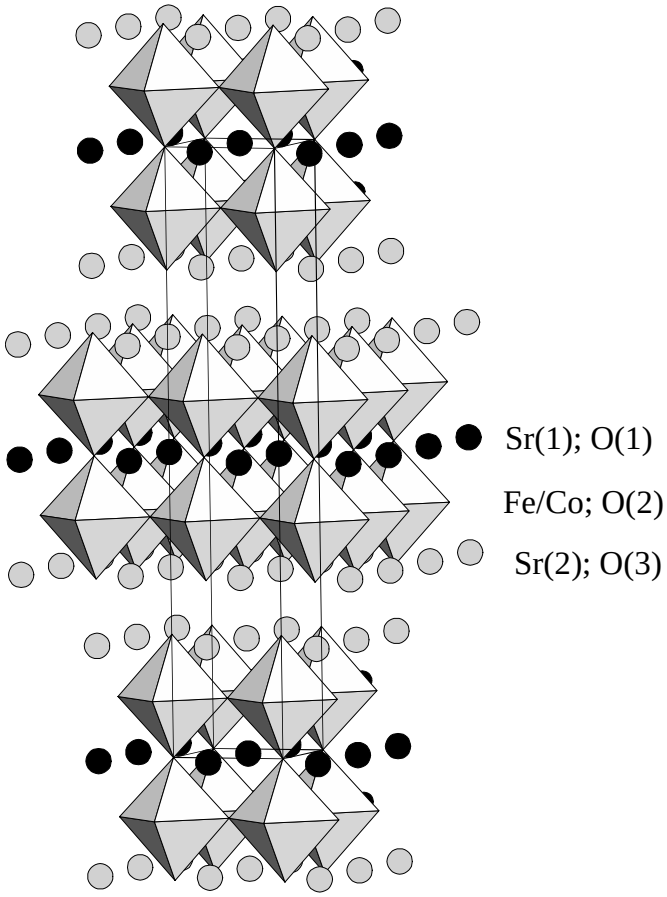

FIG. 1. The ideal $n=2$ Ruddlesden–Popper structure. The shaded octahedra are Fe/Co–O_6, while the circles represent the two crystallographically unique Sr sites.

$Sr_3Fe_{2-x}Co_xO_{7-\delta}$ promotes ferromagnetism and enhances electronic transport and MR (8–10).

Recently, in our search for new materials and to further clarify the various interactions of CMR phenomenon we (11), and others (12) have attempted to emulate the d^3/d^4 (Mn^{4+}/Mn^{3+}) interactions, in perovskite manganites with large MR, by substituting $Fe^{4+}(d^4)$ for $Mn^{4+}(d^3)$ in the $n=2$ RP manganite $Sr_3Mn_2O_7$. The resulting phases were oxygen deficient with $Mn^{3+/4+}$, $Fe^{3+/4+}$ ions, showed highly resistive, semiconducting behavior, and complex magnetic interactions with no long-range order. The Fe^{4+} ions in these phases undergo a charge localization according to: $2Fe^{4+} \rightarrow Fe^{4-\varepsilon} + Fe^{4+\varepsilon}$ (11).

We have extended these studies of $Fe^{4+}(d^4)$ containing RP phases to a systematic investigation of a similar system, $Sr_3Fe_{2-x}Co_xO_{7-\delta}$ ($0.25 \le x \le 1.75$) to clarify the effect of Co substitution for Fe in the $n=2$ RP phase. During the course of this research, several studies on related compounds appeared in the literature (8–10). In this work, we have increased the range of Co substitution to phases in the Co-rich region (x up to 1.75) in this system, and present a more complete and detailed analysis of the electronic/magnetic properties beyond those previously reported.

2. EXPERIMENTAL

$Sr_3Fe_{2-x}Co_xO_{7-\delta}$ ($x=0.25$, 0.50, 0.75, 1.00, 1.25, 1.50, 1.75) were prepared by the solid-state reaction of $SrCO_3$ (99.9+%, Aldrich), Fe_2O_3 (Fisher Scientific) and Co_3O_4 (99.7%, Alfa-Aesar). Stoichiometric amounts of the starting reagents were ground, pelletized and fired twice at 1000°C in air for 24 h; the samples were reground and repelletized before the second sintering. The final products were obtained by annealing the samples under oxygen at 1000°C for another day and furnace cooling to 200°C under flowing oxygen. The products were then removed from the furnace, while warm, and transferred expeditiously to an argon-filled dry box. This was necessary due to the extremely hygroscopic nature of these materials, especially those with higher Co content. For the determination of the oxygen content of these materials iodometric titrations were performed in triplicate, under a blanket of argon gas, with the procedure outlined by Licci *et al.* (13).

Powder X-ray diffraction (PXD) data were collected with a SCINTAG PAD V diffractometer with Cu$K\alpha$ radiation and a liquid-N_2-cooled Ge detector. Due to the highly hygroscopic properties of these compounds a rapid (few minutes) PXD scan in air was used to establish the formation of $n=2$ RP phase by the presence of characteristic low-angle (0 0 2) reflection at $2\theta \sim 9°$. For the determination of accurate unit cell parameters and structural analysis, the PXD sample was protected from the ambient by surrounding it with epoxy and covering it with a film of Mylar. PXD data on such samples were collected with a step scan of 0.02° from 30° to 110° 2θ, over a period of 90 min. The PXD at $2\theta < 30°$ contained an intense broad amorphous peak due to the Mylar. The lattice parameters and the structure were refined with the Rietveld program GSAS (14).

Temperature-dependent magnetic susceptibility, χ, measurements were made with a Quantum Design MPMS-*XL* SQUID magnetometer. The samples were cooled to 5 K, then a magnetic field of 100, 10,000 or 50,000 G was applied and data were collected while heating from 5 to 400 K (ZFC) followed by re-cooling to 5 K (FC). To prevent the reaction of the materials with atmospheric water, the samples for the magnetic measurements were all prepared in a dry box, immersed in liquid nitrogen and transferred to the SQUID. Magnetization measurements were performed with an applied field (H) of $-5\,T < H < 5\,T$. Hysteresis measurements were performed at 5 K and at the temperature ($T \sim 45$ K) where the maximum in the FC susceptibility occurred.

Transport (ρ vs T) measurements were performed in a Quantum Design (MPMS-*XL*) magnetometer with

External Device Control and Keithley equipment with standard four-probe technique at $H=0$ and 5 T. Gold wire contacts were attached to the sintered polycrystalline samples with silver paint. Care was taken to minimize air exposure of the samples during contact mounting; however, some exposure could not be avoided. The ρ vs T of the $x=1.75$ member of $Sr_3Fe_{2-x}Co_xO_{7-\delta}$ could not be measured, due to the extreme hygroscopy of the compound.

Mössbauer studies were performed with a ^{57}Co:Rh source (50 mCi) and a conventional constant acceleration Mössbauer drive. The spectra of $Sr_3Fe_{2-x}Co_xO_{7-\delta}$ ($0.25\leq x\leq 1.75$) at 4.2 and 200 K were analyzed and least square fitted by a computer program, which allowed a distribution of magnetic hyperfine fields in the 4.2 K spectra, and a distribution of quadrupole interactions in the 200 K spectra.

The X-ray absorption spectroscopy (XAS) measurements were made on beam lines X-19A and X-18B at the Brookhaven National Synchrotron Light Source with double-crystal [Si (311) or Si (111)] and channel-cut [Si (111)] monochromator, respectively. The XAS samples were protected from the ambient the same way as the PXD samples, i.e., covered with epoxy and Mylar. For transport to the synchrotron, they were sealed in several Ziploc plastic bags in the dry box and placed in a parafilm-sealed container with desiccant. Electron yield, fluorescence mode and transmission mode XAS measurements were made simultaneously and checked for consistency. A standard was run simultaneously with all measurements for precise calibration. The relative energies between various spectra were established by careful comparison of the standard spectra. In general, the relative accuracy of the energy is about ± 0.05 eV. All spectra were normalized to unity step in the absorption coefficient from well below to well above the edge.

3. RESULTS AND DISCUSSION

3.1. Powder X-Ray Diffraction

Analysis of the PXD data indicates that all compositions of $Sr_3Fe_{2-x}Co_xO_{7-\delta}$ ($0.25\leq x\leq 1.75$) prepared are isostructural with the parent compound $Sr_3Fe_2O_{7-\delta}$. All of the compounds are extremely sensitive to atmospheric moisture, therefore they were stored in a dry box at all times. When any of the samples, especially those with $x>0.75$, are left out in the ambient for more than about 15 min, the PXD shows the systematic disappearance of the (002) reflection at $2\theta\sim 9^\circ$ and the appearance of a reflection at $2\theta\sim 6^\circ$. The process is reversible, as upon reheating the sample to 1000°C and cooling it to room temperature, the (002) reflection reappears in the PXD.

Rietveld refinements were carried out in the tetragonal space group $I4/mmm$ with the atomic positions of $Sr_3Fe_2O_{7-\delta}$ (15) as starting parameters. The background was modeled with a Chebyschev polynomial of the first kind and the peak shapes were described with a pseudo-Voigt function. Due to the brevity of the scan and the difficulty in locating O with X rays the metal–oxygen distances could not be determined accurately. The PXD of $Sr_3Fe_{1.75}Co_{0.25}O_{7-\delta}$. shown in Fig. 2 is representative of these compounds. The refined lattice parameters listed in Table 2 are close to those of the corresponding $Sr_3Fe_{2-x}Co_xO_{7-\delta}$ compounds reported previously (8–10). In the inset of Fig. 2, the decrease of lattice parameters with increasing x is consistent with the smaller effective ionic radius of Co^{3+}/Co^{4+} ($r_{eff}=0.685/0.67$ Å) compared to those of Fe^{3+}/Fe^{4+} ($r_{eff}=0.785/0.725$ Å) (16, 17). However at $x>1.25$ the c cell parameter appears to increase with increasing x (Table 1; Fig. 2, inset). This behavior is attributed to increasing amounts of oxygen defects (δ, Table 1) in the compounds (15, 18). It has been well established that the oxygen vacancies are located on the O(1) site (Fig. 1), between two perovskite layers (15); these defects lead to loss of metal–oxygen–metal interactions via superexchange, and repulsion between highly charged cations along the c direction.

3.2. Chemical Analysis

The results of the iodometric titrations demonstrate that the $Sr_3Fe_{2-x}Co_xO_{7-\delta}$ phases are oxygen deficient, consistent with previous findings that it is difficult to stabilize Fe and Co in oxides with 4+ formal oxidation state, without the use of high oxygen pressures. With increasing Co

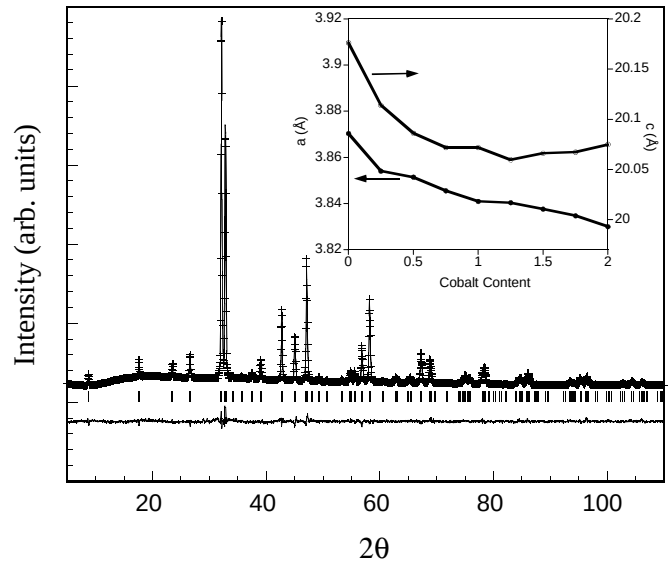

FIG. 2. X-ray diffraction data; observed (+), calculated (solid line) and allowed reflections (tics) for the compound $Sr_3Fe_{1.75}Co_{0.25}O_{6.92}$. The difference plot is at the bottom.

TABLE 1
Unit-Cell Parameters and Volume, and Oxygen Deficiency, δ in $Sr_3Fe_{2-x}Co_xO_{7-\delta}$

x	δ	a (Å)	c (Å)	V (Å^3)
0.00[a]	0.42	3.8704	20.1763	302.241
0.25	0.08	3.8541(2)	20.1140(4)	298.775
0.50	0.11	3.8505(2)	20.0861(4)	297.803
0.75	0.23	3.8456(2)	20.0721(12)	296.839
1.00	0.29	3.8410(2)	20.0720(17)	296.128
1.25	0.41	3.8404(2)	20.0595(14)	295.851
1.50	0.50	3.8376(2)	20.0662(13)	295.518
1.75	0.49	3.8348(5)	20.0675(40)	295.106
2.00[b]	0.94	3.830	20.075	294.487

[a] $Sr_3Fe_2O_{6.58}$ data from Dann *et al.* (15).
[b] $Sr_3Co_2O_{6.06}$ data from Dann *et al.* (19).

content the level of oxygen deficiency increases (Table 1). The end members of the series $Sr_3Fe_2O_{7-\delta}$ (15) and $Sr_3Co_2O_{7-\delta}$ (19) were also reported to be oxygen deficient.

3.3. Mössbauer

The Mössbauer spectra of $Sr_3Fe_{2-x}Co_2O_{7-\delta}$ at 200 K, shown in Fig. 3 exhibit at least two broad quadrupole doublet sub-spectra corresponding to a significant distribution of inequivalent iron sites. The isomer shifts (IS) are in a narrow range (from -0.1 mm/s to $+0.15$ mm/s) and indicate that these iron ions assume averaged valence states not too far removed from Fe^{4+} (see below). They differ in IS and quadrupole splitting ($\frac{1}{2}$eqQ ranging from 0 to 0.5 mm/s), according to their nearest-neighbor local environment.

In contrast, the Mössbauer spectra at 4.2 K, Fig. 4, exhibit well-defined two magnetic sextets, the parameters of

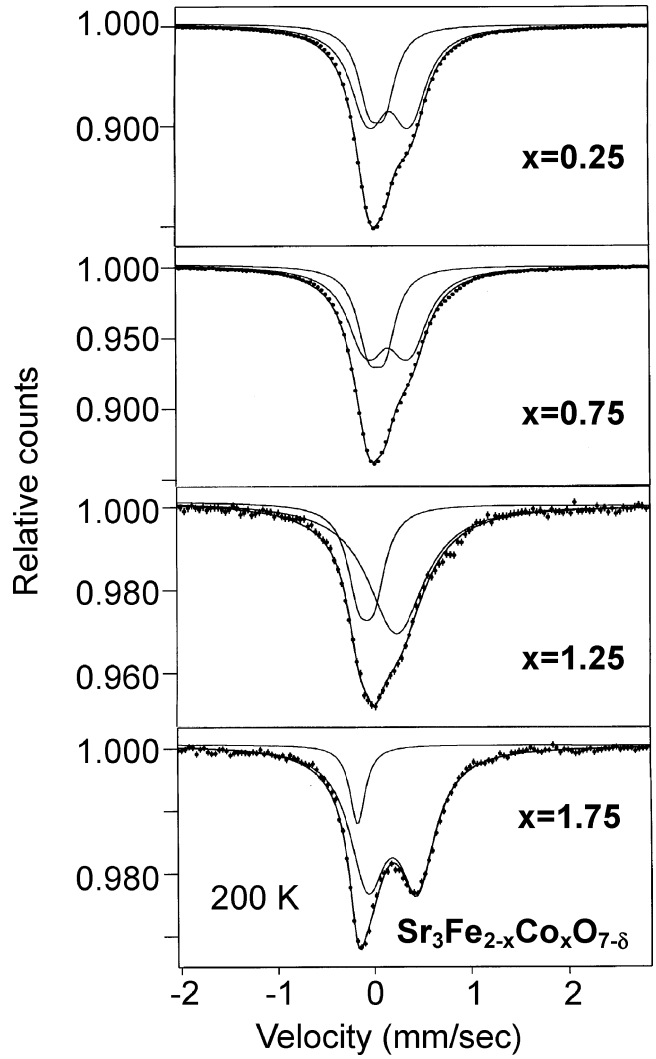

FIG. 3. Mössbauer data of $Sr_3Fe_{2-x}Co_xO_{7-\delta}$ at 200 K.

TABLE 2
Curie, C and Weiss, θ Constants, Temperature Range, T_{range} Used for the Determination of μ_B(exp), μ_B(theo),[a,b] Curie Temperature, T_c (K) and the Coercive Field at 5 K, $H_c^{5\,K}$

x	δ	$C^{exp}_{(emu/mol)}$	θ (K)	T_{range} (K)	μ_B(exp)[c]	μ_B(theo)	T_c (K)	$H_c^{5\,K}$ (T)
0.25	0.08	6.82	167	220–400	7.38	7.26[a]	160	1.02
0.50	0.11	6.73	164	220–400	7.33	7.48[a]	160	1.07
0.75	0.23	5.77	193	260–400	6.80	6.61[b]	160	1.00
1.00	0.29	5.41	199	250–400	6.58	6.22[b]	190	0.22
1.25	0.41	4.94	173	260–400	6.31	5.74[b]	190	0.29
1.50	0.50	4.02	198	220–400	5.67	5.41[b]	195	1.50
1.75	0.49	3.42	187	250–400	5.23	5.58[b]	195	2.53

[a] $\mu_{theo} = \sqrt{8\{xC_{Co^{4+}_{HS}} + (2-x)[(1-f)C_{Fe^{3+}} + fC_{Fe^{4+}}]\}}$.

[b] $\mu_{theo} = \sqrt{8\{(2-x)C_{Fe^{4+}} + x[(1-f)C_{Co^{3+}_{LS}} + fC_{Co^{4+}_{HS}}]\}}$.

[c] $\mu_{exp} = \sqrt{8C_{exp}}$.

which appear in Table 3. The absorption lines in the 4.2 K spectra, Fig. 4, are significantly broadened, presumably due to the spread in isomer shifts and quadrupole interactions observed in the spectra above the magnetic ordering temperature of the materials (Fig. 3). In addition, the magnetic hyperfine fields have a considerable distribution, in particular the high Fe concentration samples, indicating cluster-glass characteristics in the magnetic order.

In Fig. 5, we plot our Mössbauer isomer shift results (Sites I, II, and average isomer shift $\langle IS \rangle$) at 4.2 K vs Co composition, x. The distributions of isomer shift values at 200 K, for the $x<1.0$ samples, are indicated by the rectangle boxes (labeled 200 K) in the figure. In Fig. 5, we also compare our present results to literature values for $AFe^{4+}O_3$ (A = Ca and Sr), $LaFe^{3+}O_3$ (20), $La_2LiFe^{5+}O_6$ (21) and finally for $Sr_3Fe_{2-x}Mn_xO_{7-\delta}$, $x=0.66$ from our

TABLE 3
Hyperfine Interaction Parameters of ^{57}Fe in $Sr_3Fe_{2-x}Co_xO_{7-\delta}$, the Error Bars of Intensity Are 5%, of Isomer Shift Are 0.04 mm/s, of Quadrupole Interaction ($\frac{1}{2}eqQ$) Are 0.05 mm/s and of Hyperfine Field Are 10 kOe

x	Intensity (%)	Isomer shift (mm/s)	Quadrupole interaction (mm/s)	Magnetic hyperfine field (kOe)
0.25	54	0.04	—	285
	46	0.31	—	424
0.75	57	0.05	—	326
	43	0.25	−0.24	420
1.25	79	0.09	—	320
	21	0.43	−0.28	469
1.75	80	0.09	—	310
	20	0.38	—	465

previous work (11). The results on $Sr_3(Fe/Co)_2O_{7-\delta}$ are similar *in part* to our previous work on the RP [SrO][$Sr(Fe_xMn_{1-x})O_3$]$_n$ ($n=2$, 3 and ∞) compounds (11, 22, 23), namely the average valence over all sites appears to be close to 4+ and the Fe–O covalency is strong with two Fe sites, each of which are admixtures of Fe^{3+}, Fe^{4+} and (to a small extent) Fe^{5+}. The XAS results (discussed below) support both the strong covalency and close-to-Fe^{4+} behavior; however they do not resolve the two-site behavior indicated by the Mössbauer data. There is, however, an important difference between the $Sr_3Fe_{2-x}Mn_xO_{7-\delta}$ and $Sr_3Fe_{2-x}Co_xO_{7-\delta}$ substituted systems. Specifically, compare the *small* IS distribution (see the $T=200$ K boxes in Fig. 5) for the $x<1.0$, Co-substituted materials to the *large* IS distribution at 200 K for $Sr_3Fe_{2-x}Mn_xO_{7-\delta}$, $x=0.66$. It is apparent from this comparison that while the Mn–substitution promotes strong Fe–localization, the Co substitution allows a much greater Fe–hybridization, itinerancy and the concomitant FM interactions. We will revisit this point in the conclusion.

3.4. *X-Ray Absorption Spectroscopy*

X-ray absorption near-edge spectroscopy was used to further characterize the formal oxidation state of the transition metal ions in the $Sr_3Fe_{2-x}Co_xO_{7-\delta}$ series.

To clarify the role of covalent *d*-configuration mixing in 3*d* row K-edge XAS, we compare the K edges of Zn and Cu in a perovskite-based $(La_{1-x}Sr_x)(Cu_{1-y}Zn_y)O_{4-\delta}$ compound in Fig. 6 (24). The main K edges of 3*d* transition metal compounds are dominated by transitions into empty 4*p* states, as is well illustrated by the strong B feature in the

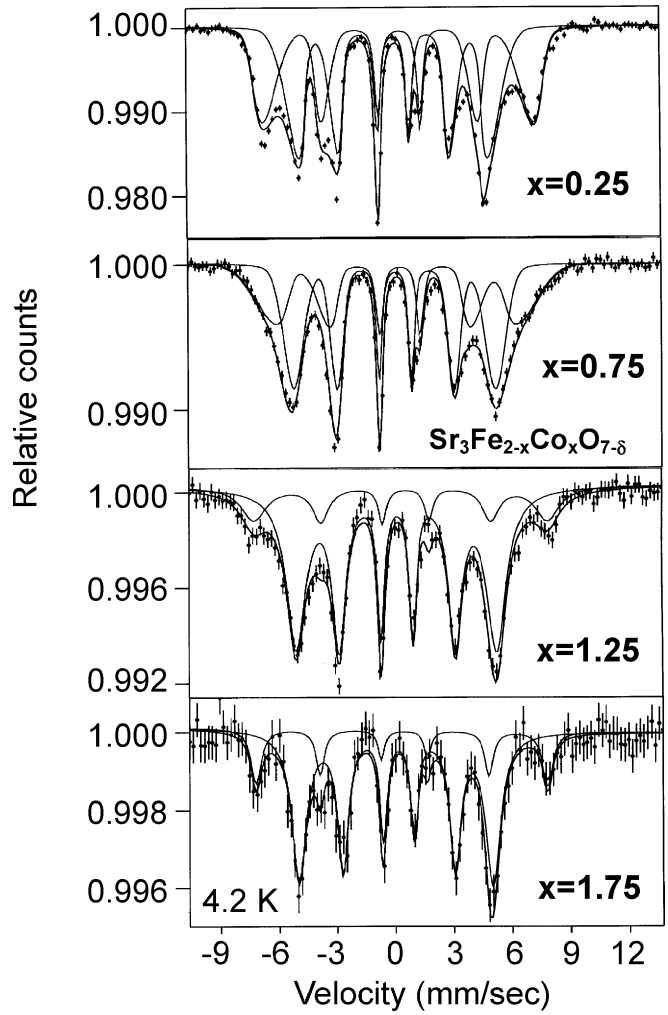

FIG. 4. Mössbauer data of $Sr_3Fe_{2-x}Co_xO_{7-\delta}$ at 4.2 K.

Zn–K spectrum in Fig. 6. In the Cu–K spectrum, in Fig. 6, the 4*p* feature is clearly split into at least two features, B_1 ($d^{10}L$, where the L denotes an O–ligand hole), and B_2 (d^9). Within the cluster model interpretation, these features arise from the mixing of these two *d*-configurations due to Cu–O covalency (25, 26). The single intense B feature of Zn^{2+} reflects its stable d^{10} configuration.

Figures 7 and 8 show the Fe/Co–K main edges for selected $Sr_3(Fe,Co)_2O_{7-\delta}$ phases along with a series of standard compounds. The perovskite-based Fe^{3+} and Co^{3+} *standard* spectra exhibit a rather robust B_1 feature (Figs. 7 and 8, bottom). The Fe^{4+} and Co^{4+} standard spectra, on the other hand, exhibit strong Fe/Co–O covalency effects and a stronger superposition of *d* configuration features in their K-edge spectra. Specifically (as in the Cu spectrum in Fig. 6), these Fe^{4+}/Co^{4+} spectra exhibit much-reduced B_1 features compared to the B_2 features. This trend is emphasized in the $Sr(Fe,Sc)O_3$ spectrum in Fig. 8 (bottom), where the Sc^{3+} substitution

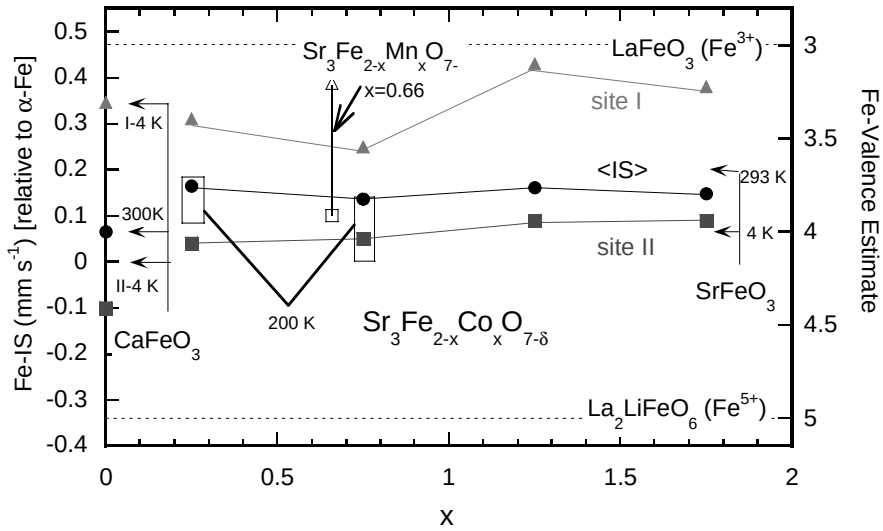

FIG. 5. The Mössbauer isomer shifts (for Sites I, II and the average, $\langle$ IS $\rangle$ at 4 K) for $Sr_3Fe_{2-x}Co_xO_{7-\delta}$ vs x. Literature results along with a nominal Fe-valence scale are also included. The isomer shifts for $CaFeO_3$ and $SrFeO_3$ were obtained from (33), for $LaFeO_3$ from (20), for La_2LiFeO_6 from (21) and finally for $Sr_3Fe_{2-x}Mn_xO_{7-\delta}$, $x=0.66$ were from our previous work (11).

induces a decreasing weight for the lower-d Fe configuration (i.e., Fe^{5+}-(d^3) for every Sc^{3+} substituted for Fe^{3+}) and the B_1-feature intensity is accordingly still further reduced.

From the above, one signature of increasing formal oxidation state of Fe and Co in such compounds is a reduction of the B_1-feature intensity. A second, coupled signature is the chemical shift of the edge to higher energy. Comparing the Fe/Co–K edge *standard* spectra at the absorption coefficient, $\mu = 1.0$ value (in Figs. 7 and 8, bottom) one notes a modest, but discernable chemical shift of the Fe^{4+}/Co^{4+} standards to higher energy (relative to the Fe^{3+}/Co^{3+} standards).

Turning to the $Sr_3(Fe,Co)_2O_{7-\delta}$ spectra (in Figs. 7 and 8, top), both the reduced intensities of the B_1 features and the chemical shifts are consistent with the Fe and Co oxidation states being well above 3+. In the case of Fe, the oxidation state appears quite close to that in $SrFeO_3$ (i.e., a formally 4+), as is consistent with the Mössbauer results herein. In

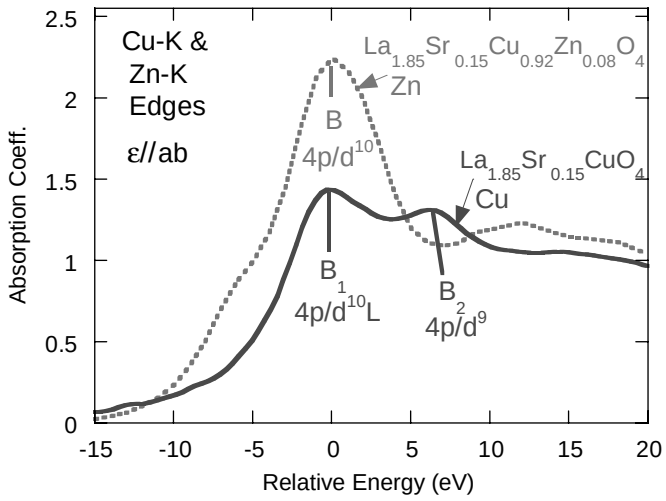

FIG. 6. A comparison of the Zn and Cu K edges at similar octahedral sites in $La_{1-x}Sr_xCu_{1-y}Zn_yO_4$ based materials, from Ref. (24).

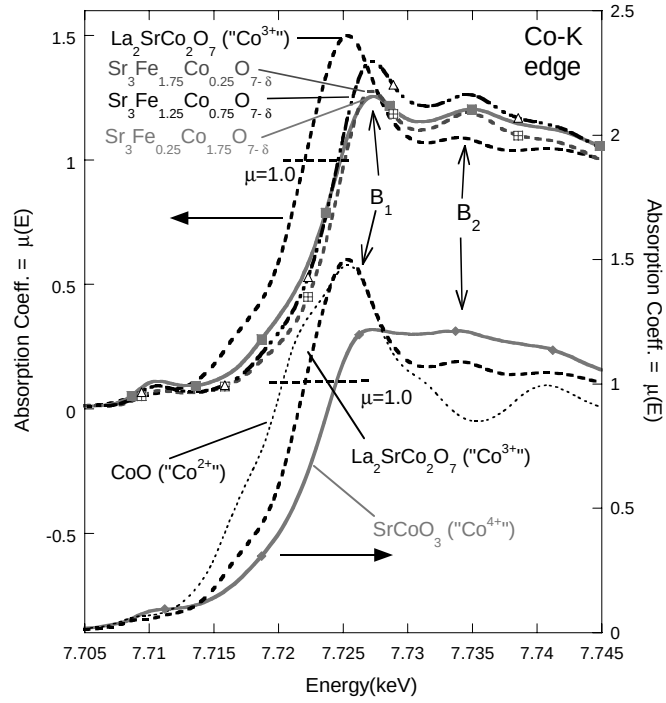

FIG. 7. The Co–K main edges of a series of Co standard compounds and selected $Sr_3(Fe,Co)_2O_{7-\delta}$ materials.

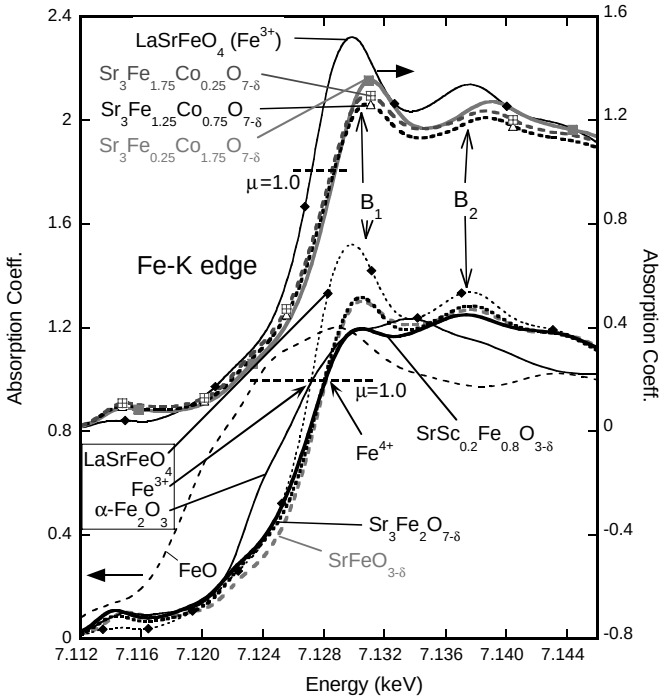

FIG. 8. The Fe–K main edges of a series of Fe standard compounds and selected $Sr_3(Fe,Co)_2O_{7-\delta}$ materials.

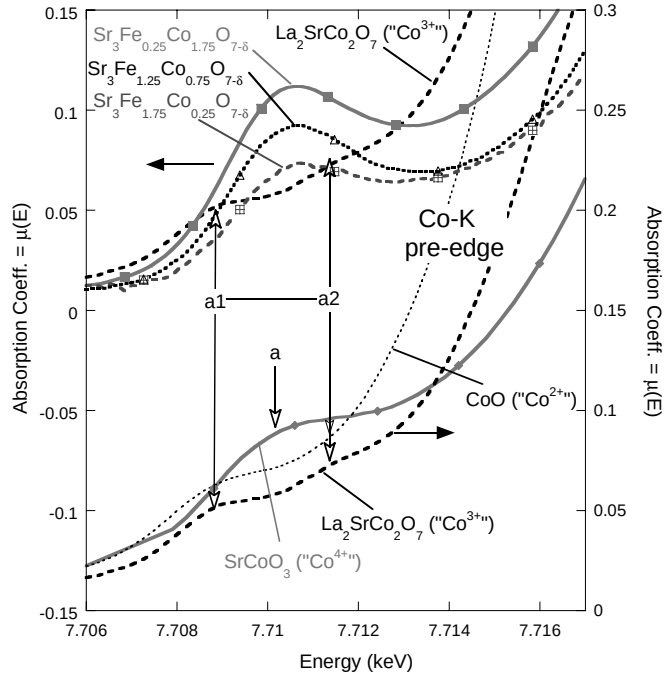

FIG. 9. The Co–K pre-edges of a series of Co standard compounds and selected $Sr_3(Fe,Co)_2O_{7-\delta}$ materials.

the case of Co, comparison to the $SrCoO_3$ spectrum (specifically note the intensity of the B_1 feature) indicates that the Co valence involves a higher degree of 3+ admixture, as argued previously herein.

The K pre-edge features of 3*d*-row elements involve unoccupied 3*d* final states via quadrapole and dipole (by inter-site *d*/*p* hybridization) transitions. In the case of the Co^{3+} standards, the pre-edge (Fig. 9, bottom) exhibits a resolved, *low-intensity* bimodal structure (note the a1–a2 features). The Co^{4+} pre-edge of the $SrCoO_3$ standard manifests a much more intense single a feature. The Co–K pre-edges for the $Sr_3(Fe,Co)_2O_{7-\delta}$ spectra appear more typical of the Co^{4+} standards (Fig. 9, top) however, the weak Co^{3+} pre-edge intensity would make its presence difficult to observe. The Fe^{3+} standard pre-edges (Fig. 10, middle) exhibit double b1–b2 features, with a small b3 feature also occurring for Fe_2O_3. The Fe^{4+} standard pre-edges (Fig. 10, bottom) manifest a more intense single b feature. The Fe pre-edges for the $Sr_3(Fe,Co)_2O_{7-\delta}$ spectra (Fig. 10, top) are essentially typical of the Fe^{4+} standards.

Thus the Fe/Co–K XAS main and pre-edge spectra support formal oxidation states for both the Fe and Co sites in the $Sr_3(Fe,Co)_2O_{7-\delta}$ materials well above 3+. The Fe oxidation state appears close to that of Fe in $SrFeO_{3-\delta}$ while the valence state of Co involves a greater degree of 3+ admixture consistent with our magnetic and Mössbauer results. The strong covalency and mixed *d*-configuration character of the Fe/Co electronic states in these materials is apparent in the XAS results. This strong covalency complicates an accurate determination of the oxidation states from XAS, and it also emphasizes that a simple valence assignment may be inappropriate for these materials.

3.5. *Electrical Resistivity*

Figure 11 shows temperature-dependent resistivity (a) and magnetoresistance (b) of $Sr_3Fe_{2-x}Co_xO_{7-\delta}$. The resistivity ρ was normalized to that at 300 K, ρ_{300}, in an effort to eliminate the effect of the density of the sintered samples. Our attempts to fit the resistivity to various exponential laws led us to the conclusion that the resistivity in the whole temperature range (5–300 K) cannot be described by a single law. The best fit was obtained above 80 K with Mott's law describing variable range hopping with states localized near the Fermi level (27):

$$\rho = \rho_0 \exp[(T_0/T)^{1/4}], \qquad [1]$$

where $T_0 \propto 1/[\xi^3 N(E_F)]$, ξ is the localization length and $N(E_F)$ is the density of states near the Fermi level. The fit of the resistivity data to Eq. [3] suggests Anderson localization due to electronic disorder in these compounds. Anderson localization could be due to Fe/Co or oxygen vacancy disorder, or both. Such disorder cannot be observed by X-ray powder diffraction; hence, neutron

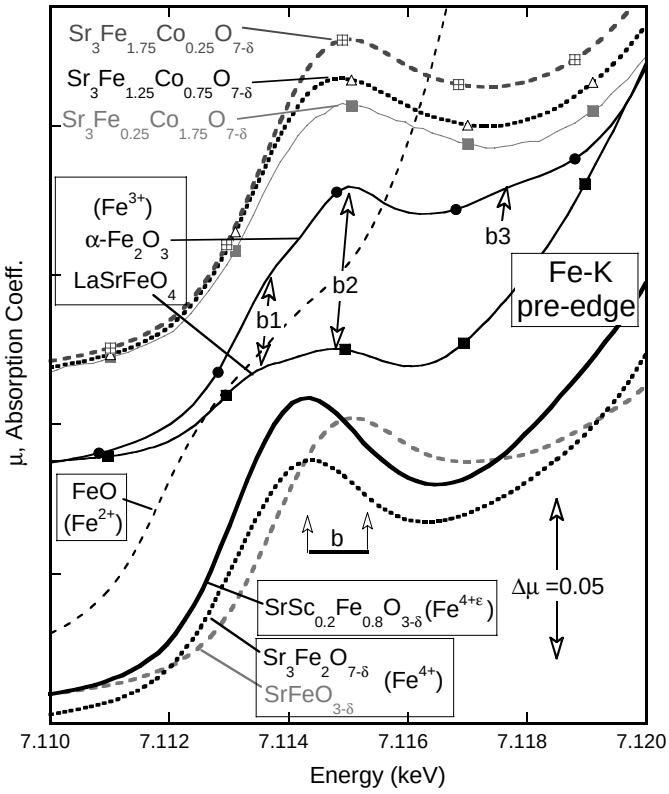

FIG. 10. The Fe–K pre-edges of a series of Fe standard compounds and selected $Sr_3(Fe,Co)_2O_{7-\delta}$ materials.

diffraction studies would be useful in elucidating this problem.

As mentioned above, the exp-$T^{-1/4}$ dependence of ρ is linear above 80 K (Figs. 12 and 13). T_0's extracted from the plots in the temperature range of 80–180 K are presented in Table 4. T_0 is inversely proportional to the cube of localization length and the density of states; for the sake of comparison we assume that the density of states is constant for the series of compounds. Then higher T_0 values represent a higher degree of electron localization. T_0 is a minimum for an Fe:Co ratio 1:1, which indicates that the conductivity at higher temperatures is facilitated by a statistically higher number of Fe–O–Co pathways. However, T_0 can also be influenced by the variable oxygen content in the $Sr_3Fe_{2-x}Co_xO_{7-\delta}$ series, where δ monotonically increases with increasing x.

At lower temperatures (below 45 K) the best fit to the resistivity data can be obtained again by considering a variable range hopping mechanism. However, the T_0 values are much lower in this case (Table 4), which suggest a lower degree of electron localization. The change in resistivity behavior around 45 K in Fig. 12 indicates that some change(s) are occurring in the electron hopping conditions, or the electronic structure, leading to a dramatic decrease of T_0's and lower resistances than expected from the higher-temperature trends. Coincidentally, the change in the resistivity at $\sim$45 K corresponds to the temperature where the down turn in the FC susceptibility observed presumably corresponds to the cluster-glass freezing temperature, Fig. 14 (discussed below). Thus the broad change in transport properties evidenced around $\sim$45 K is consistent with increased delocalization of electrons at the cluster-glass transition. Moreover, if FM domains dominate the cluster-glass transition, as they appear to dominate in the region below $\sim$200 K, then FM interactions lead to lower electron scattering as manifested by the lower T_0's, enhanced hopping and lower ρ.

3.6. *Magnetic Susceptibility*

The temperature-dependent susceptibility, χ, shown in Fig. 14 for each compound, shows a significant deviation between the FC and ZFC data, similar to the results reported previously for $Sr_3(Fe/Co)_2O_{7-\delta}$ compounds (8–10). The Curie, C and Weiss, θ constants were determined from the high-temperature χ vs T data, Fig. 14, inset. The positive values of θ for all of the phases studied here suggest that FM interactions dominate. While spin-glass systems typically exhibit differences in the FC/ZFC

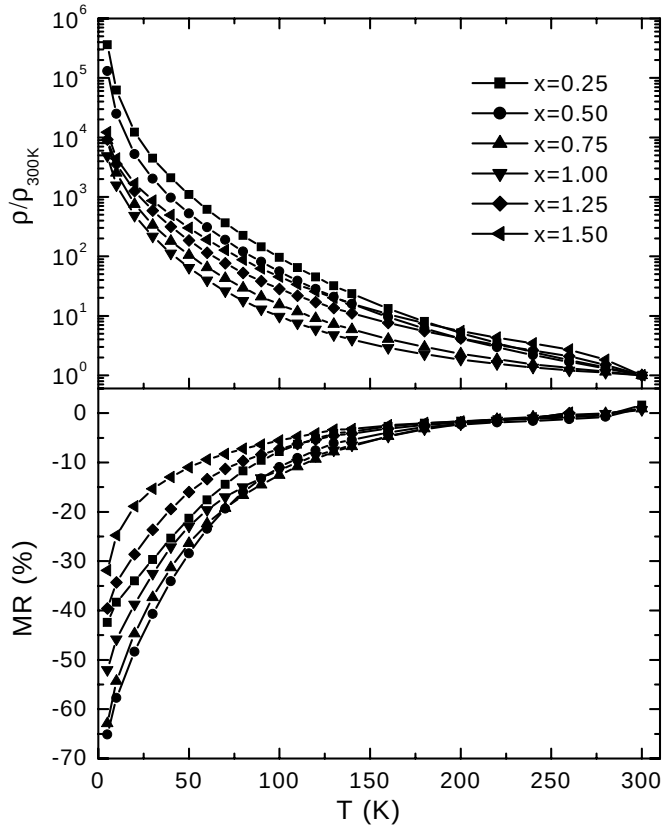

FIG. 11. Normalized resistivity (a) and magnetoresistance (b) of $Sr_3Fe_{2-x}Co_xO_{77-\delta}$.

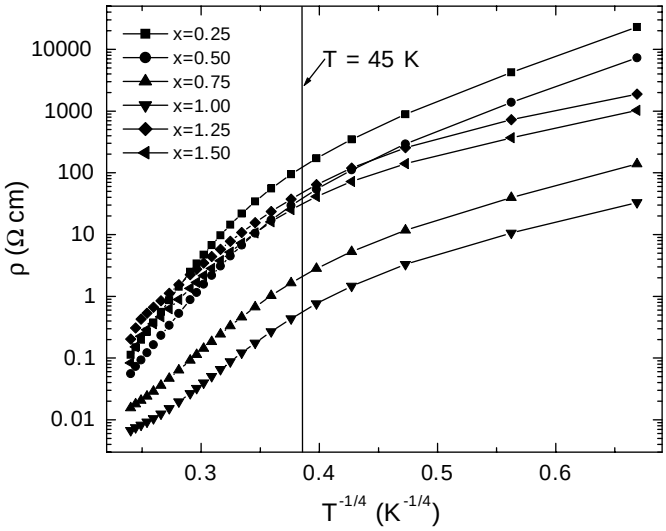

FIG. 12. $1/T^{1/4}$ dependence of the resistivity of $Sr_3Fe_{2-x}Co_xO_{7-\delta}$.

susceptibilities below the ZFC susceptibility maximum, in this system (see Fig. 14) these susceptibilities are different to far higher temperatures. Indeed, the ZFC and FC low field susceptibility curves "merge" at a temperature (T_M) comparable to the FM-like θ value.

A significant difference in the temperature-dependent magnetic susceptibility of $Sr_3Fe_{0.75}Co_{1.25}O_{6.59}$ is observed when the data are collected in different applied magnetic fields, Figs. 14e and 14h. It should be noted that the susceptibility curves, in different fields (Fig. 14h), "merge" at the same temperature where the FC and ZFC curves merge (Fig. 14e) consistent with FM-cluster effects. The deviations between the ZFC and FC susceptibility data are greatly reduced in high fields (Fig. 14h), apparently as the field-forced cluster alignment overcomes the frustrating inter-cluster interactions. Indeed full cluster alignment is presumably reflected in the full coincidence between the ZFC and FC susceptibility data measured in an applied field of 50,000 G (Fig. 14h).

The deviation between the FC and ZFC data has been observed before in other B-site substituted $n=2$ RP phases, and has been attributed to transition (T_{SG}) to a spin-glass or cluster-glass-type state (11, 12, 18, 22). The random distribution of B cations ($Fe^{3+/4+}$ and $Co^{3+/4+}$) in these compounds leads to complex magnetic interactions and fluctuating FM and AFM domains. The size of these domains increases/decreases with cooling/heating as well as applied magnetic field strength, and results in the observed differences between the FC and ZFC susceptibility data.

The magnetic properties were further investigated by magnetization measurements. The experimentally determined effective magnetic moments μ_{exp} in Table 2 were compared to the predicted values of the spin-only formulas:

$$\mu_{theo} = \sqrt{8\{xC_{Co_{HS}^{4+}} + (2-x)[(1-f)C_{Fe^{3+}} + fC_{Fe^{4+}}]\}} \quad [2]$$

or

$$\mu_{theo} = \sqrt{8\{(2-x)C_{Fe^{4+}} + x[(1-f)C_{Co_{LS}^{3+}} + fC_{Co_{HS}^{4+}}]\}}, \quad [3]$$

where C is the theoretical Curie constant for the metal cation and f is the fraction of Fe^{4+} and Co_{HS}^{4+} in Eqs. [2] and [3], respectively, and x corresponds to the chemical formula. In the calculations above, one of the B cations was constrained to be 4+, while the other cation was allowed to be 3+ and 4+. The relative amounts of 3+ and 4+ cations were based on the oxygen content as determined iodometrically. The calculated μ_{theo} obtained by either Eq. [2] or [3], which was closest to the experimentally determined μ_{theo} is given in Table 2. There is excellent agreement between the experimental and theoretical μ_{theo} values. For all of the compounds, with the exception of $x=0.25$ and 0.50, the best fit of the experimental μ_{theo} values is obtained assuming a mixed oxidation state of $Co^{3+/4+}$ and Fe^{4+} (Table 2). These results are not surprising in the light of the difficulty in stabilizing $Co^{4+}(d^5)$ compared to low-spin $Co^{3+}(d^6t_{2g})$.

The random distribution of Co and Fe within the compounds results in FM interactions between Fe^{4+}–O–Co^{4+}, as well as AFM superexchange-type interactions between the metal cations via the intervening oxygen ions for Fe^{4+}–O–Fe^{4+}, Co^{4+}–O–Co^{4+} and Co^{3+}–O–Co^{3+} (28, 29). The presence of multiple kinds of exchange interactions leads to the observed cluster-glass-type magnetism.

Field-dependent magnetization data for $Sr_3Fe_{0.5}Co_{1.5}O_{6.50}$ are shown in Fig. 15 top. For all compositions studied similar field-dependent magnetization plots were obtained. At 5 K there is a pronounced hysteresis observed for all the compounds, but no saturation of the magnetic moments is observed even in an applied field of 5 T, Fig. 15, top, similar to the results reported previously for $Sr_3(Fe/Co)_2O_{7-\delta}$ compounds (8–10). The coercivity (H_c) of each compound at 5 K is listed in Table 2. M–H loops measured at the temperature corresponding to the maximum observed in the FC data are sigmoidal with no observed hysteresis, Fig. 15, top. At 250 K the M–H plots are linear, Fig. 15, top. The hysteresis observed at 5 K for these compounds confirms that the magnetic interactions are primarily FM, consistent with the results of the Curie–Weiss fits. For compounds in which the Fe:Co ratio is approximately 1:1 there appear to be a greater number of FM-type interactions, which results in a higher saturation moment per transition metal ion than for compounds with larger amounts of one metal ion relative to the other (Fig. 16). This behavior is attributed to significantly larger

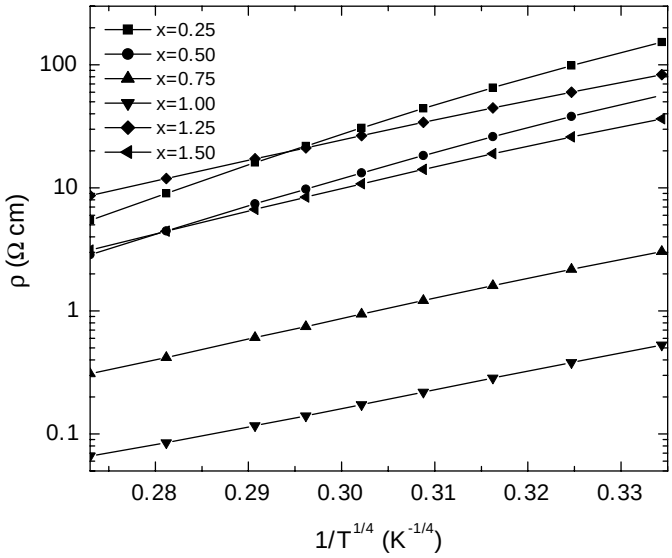

FIG. 13. $1/T^{1/4}$ dependence of the resistivity of $Sr_3Fe_{2-x}Co_xO_{7-\delta}$ in the temperature range of 80–180 K.

numbers of AFM superexchange-type interactions in the $x<1$ and $x>1$ compounds.

3.7. Magnetoresistance

The considerations on the electronic transport properties are also supported by the MR behavior of these materials. The application of a magnetic field further increases the number of FM domains and the probability of hopping, virtually eliminating AF interactions (Fig. 15, top) and giving rise to the observed intra-grain MR (Fig. 11b). Moreover, inter-grain MR, as expected, is also evident in Fig. 15, bottom. In addition, inter-planar tunneling effects may also be expected (30). The total MR observed could originate from all these mechanisms (Fig. 11b). The overall magnitude of MR for our compounds with corresponding Fe/Co ratios is larger than that reported for $Sr_3Fe_{1.8}Co_{0.2}O_{\sim 7}$ (8) and $Sr_3FeCoO_{6.94}$ (10) under similar conditions (i.e., H and T). Ghosh *et al.* (8) reported a $\sim -23\%$ MR at 5 T and 5 K; the MR of our compound with a similar composition, $Sr_3Fe_{1.75}Co_{0.25}O_{6.92}$, is $\sim -42\%$ under the same conditions. Bréard *et al.* (10) reported a $\sim -20\%$ MR at 5 T and 10 K; our compound with composition $Sr_3FeCoO_{6.71}$ exhibited a $\sim -46\%$ MR under the same conditions. The reduction in oxygen content and the concomitant increased atomic disorder of our samples appears to be responsible for the enhancement of MR in our materials. It has been observed before in manganites that increased FM/AFM fluctuations or electronic phase separations enhance MR (31).

The field-dependent MR data of all studied samples, with a typical example presented in Fig. 15, bottom, has two maxima. The difference between the two maxima ΔH is related to the coercive field, H_c (32) and is in good agreement with H_c obtained from the hysteresis results, which indicate $H_c \sim 0.3$–2.5 T (Table 2).

TABLE 4
Oxygen Nonstoichiometry, δ, Room Temperature Resistivity, ρ_{300}, Reduced Activation Energy, T_0, and Magnetoresistance, MR of $Sr_3Fe_{2-x}Co_xO_{7-\delta}$

x	δ	ρ_{300} (Ω cm)	T_0 ($\times 104$ K) (80–180 K range)	T_0 ($\times 104$ K) (5–40 K range)	MR (%) at 5 K and 5 T
0.25	0.08	1.10×10^{-1}	886	8.83	−42.4
0.50	0.11	5.57×10^{-2}	571	8.65	−65.2
0.75	0.23	1.57×10^{-2}	200	3.20	−62.9
1.00	0.29	6.77×10^{-3}	137	2.61	−52.1
1.25	0.41	2.04×10^{-1}	188	1.58	−39.6
1.50	0.50	8.37×10^{-2}	263	1.37	−31.9

4. CONCLUSION

We have prepared a series of oxygen-deficient Co-substituted $n=2$ Ruddlesden–Popper strontium ferrates, $Sr_3Fe_{2-x}Co_xO_{7-\delta}$ ($0.25 \le x \le 1.75$). The substitution of Fe by Co weakens the AF interactions, which are dominant in the parent compound $Sr_3Fe_2O_{7-\delta}$, and enhance FM interactions. Static or fluctuating FM domains (with a possible AF component) are manifested by cluster-type magnetic effects below ~ 200 K. Relatively large MRs are observed in all compositions (largest MR of $\sim -65\%$ for $x=0.25$). All the $Sr_3Fe_{2-x}Co_xO_{7-\delta}$ phases are semiconducting with variable-range hopping mechanism. Magnetic susceptibility, XAS and Mössbauer data indicate that the Fe ions are on-average tetravalent with a strong covalency-induced superposition of d configurations.

It is instructive to compare our current findings, for $Sr_3Fe_{2-x}Co_xO_{7-\delta}$, and our previous results, for $Sr_3Fe_{2-x}Mn_xO_{7-\delta}$, in terms of the role of suppressing/promoting inter-site transition metal hybridization, d hopping and FM super/double-exchange.

In Figs. 17a and 17b, we summarize the substitution-induced transport, magnetic and energy-scale results for these two systems. Mn substitution for Fe can be seen to decrease the hopping conductivity by up to four orders of magnitude, and suppress any FM enhancement in the susceptibility (Fig. 17a). Mn substitution also induces extremely small paramagnetic θ values, indicative of weak/frustrated magnetic interactions (Fig. 17b). Thus much of the Mn-phase diagram is dominated by low-energy-scale frustrated spin-glass behavior. These effects have been discussed previously in terms of a mismatch in the energies of the Mn and Fe d states precluding resonant hopping and mutually isolating and localizing them (11, 12, 22, 23).

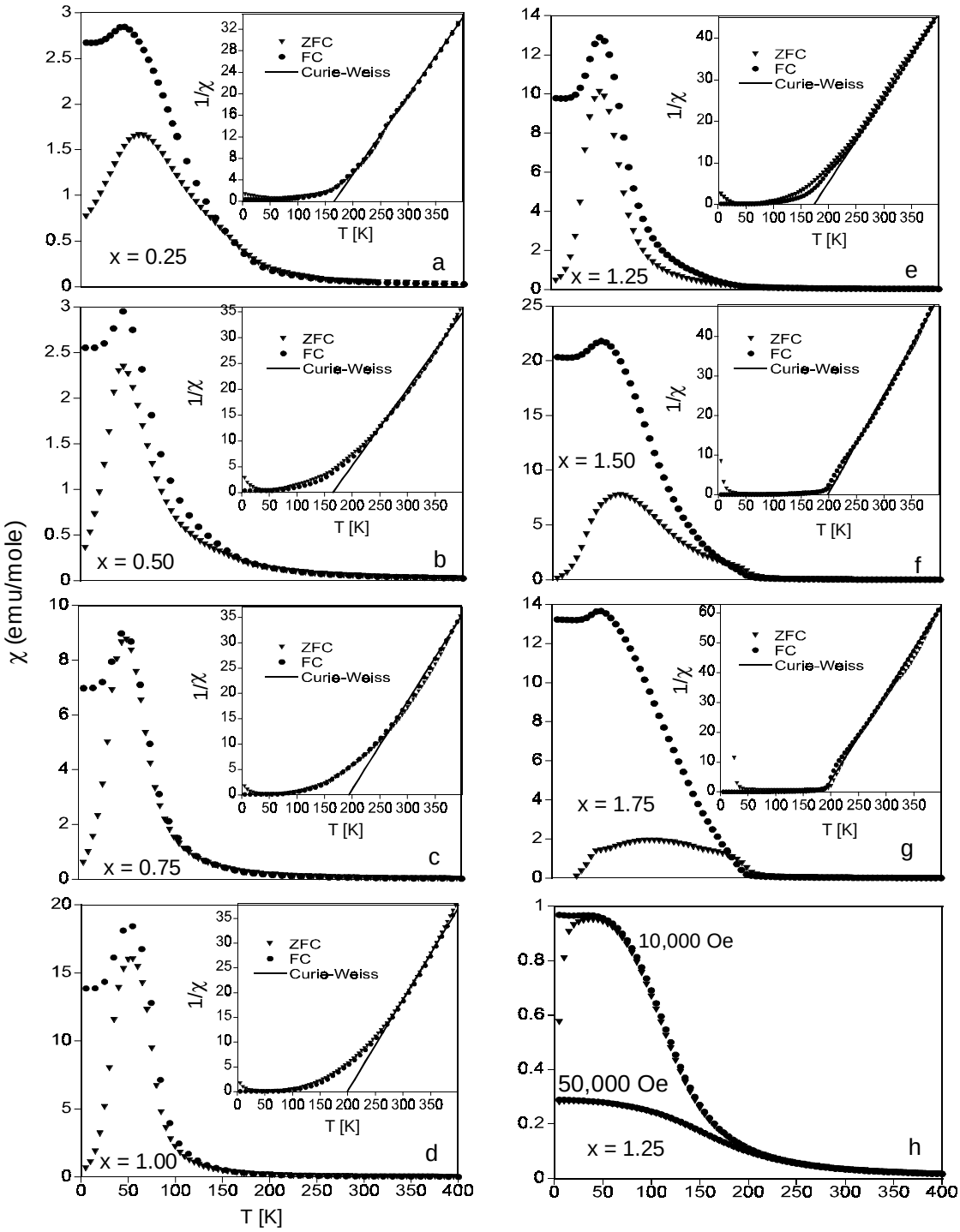

FIG. 14. Temperature-dependent magnetic susceptibility, χ, FC and ZFC for $Sr_3Fe_{2-x}Co_xO_{7-\delta}$ measured at $H = 100$ G. Note: top (e) and bottom right (h) for $Sr_3Fe_{0.75}Co_{1.25}O_{6.59}$ measured in H of 100, and 10,000 and 50,000 G, respectively. Inset: $1/\chi$ vs T for $Sr_3Fe_{2-x}Co_xO_{7-\delta}$

In contrast, the effects of the substitution of Co for Fe are dramatic. The hopping conductivity is enhanced and a robust FM enhancement of the susceptibility maximum is seen (Fig. 17a). Co substitution almost immediately (i.e., at low x) induces a strong FM-like paramagnetic θ value in the $\sim$200 K range consistent with hopping-induced double-exchange FM interactions (Fig. 17b). Indeed, the persistent enhancement of the FC (over the ZFC) susceptibility, up to a "merger" temperature (T_M in Fig. 17b) of $\sim$200 K, indicates that static, or very long-time scale FM

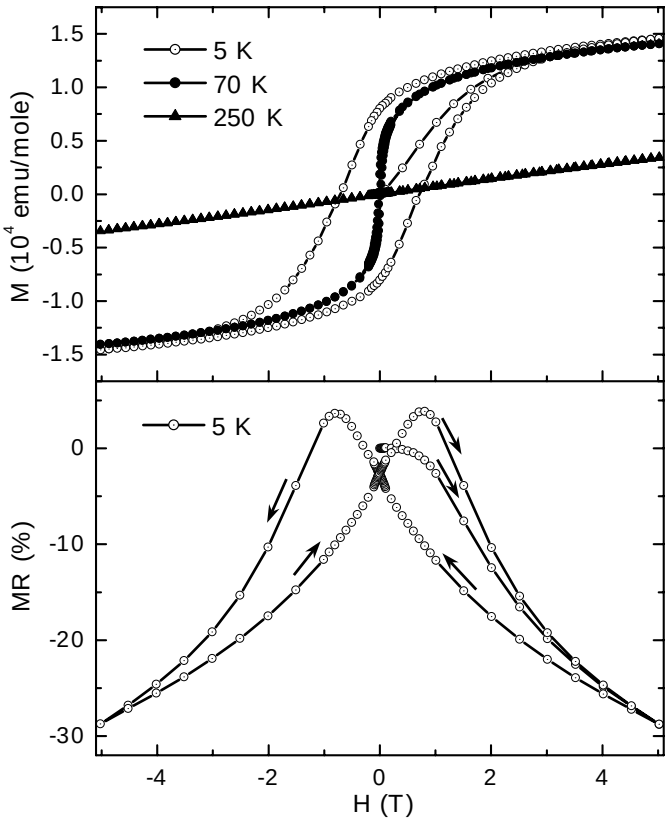

FIG. 15. Magnetization vs field plots for $Sr_3Fe_{0.5}Co_{1.5}O_{6.5}$ (top); field-dependent magnetoresistance of $Sr_3Fe_{0.5}Co_{1.5}O_{6.5}$ at 5 K (bottom).

clusters are present for all Co concentrations (Fig. 17b). The presence of lower-energy-scale (e.g., T_p (ZFC) $\sim$50–100 K in Fig. 17b) AF/frustrated interactions is also apparent from the strong peaks in the susceptibility.

In Fig. 16, the variations of the 5 T magnetization (M) and H_c (both at 5 K) with x are shown. The magnitude of the 5 T magnetization is clearly well away from full-moment saturation, indicating the presence of AF interactions and/or lower-spin Co. The downward trend of the 5 T

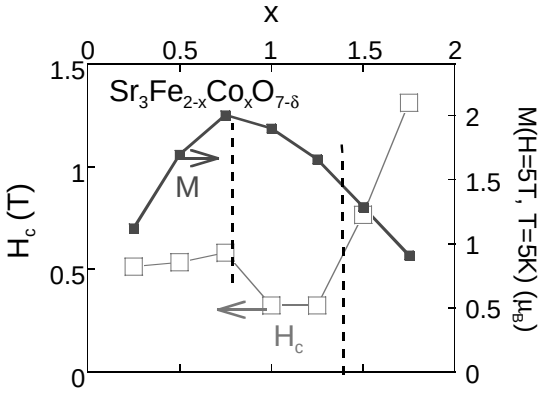

FIG. 16. The magnetization (M), at $H=5$ T and $T=5$ K, and the coercive field, H_c, vs composition for the $Sr_3Fe_{2-x}Co_xO_{7-\delta}$ system.

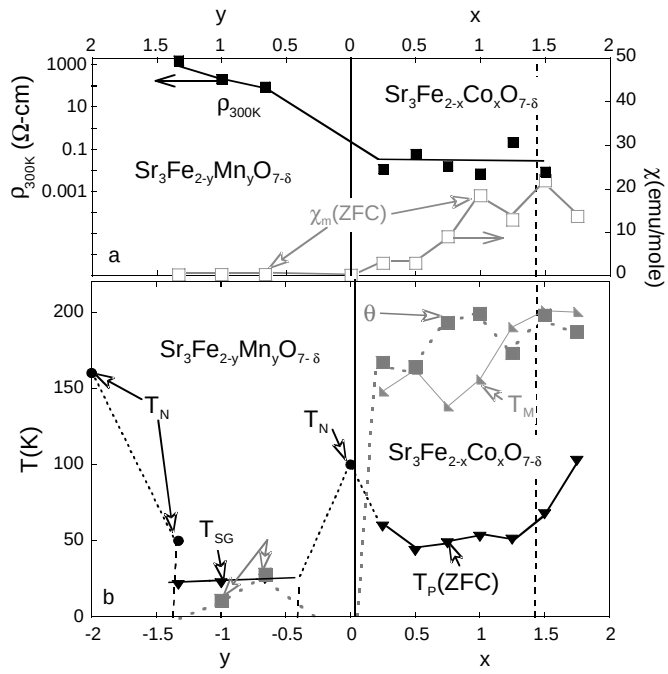

FIG. 17. A summary of the properties of the $Sr_3Fe_{2-x}Mn_xO_{7-\delta}$ and $Sr_3Fe_{2-x}Co_xO_{7-\delta}$ systems vs the substitution concentrations x and y. (a) The variation of logarithmic resistivity, ρ_{300}, at 300 K and the magnitude of the maximum of the zero-field-cooled susceptibility χ_M (ZFC). (b) Energy/temperature scales in these systems: the AF ordering temperatures, T_N; the spin-glass temperatures, T_{SG}; the temperatures of the ZFC peak in the magnetic susceptibility, T_P (ZFC); the paramagnetic Weiss temperatures, θ and the temperatures at which the zero-field and field-cooled susceptibilities merge, T_M.

magnetization for x above $\sim$0.9, and the correlated decreased H_c indicate a magnetic phase modification in this range. At higher x the H_c (Fig. 16), the T_p (ZFC) results (Fig. 17a) and the susceptibility curve evolution (Figs. 15e–g) all suggest that the magnetic phase of the materials with $x>1.4$ has changed still more in character. The increasing O deficiency at these $x>1.4$ concentrations could be important in this behavior.

In conclusion, it appears that the properties of this system are dominated by the energy matching of the Co d states to those of the Fe. This promotes (as opposed to the Mn-induced suppression) *local* inter-atomic hopping and the *local* FM interactions, which accompany it. However, the magnetic cluster effects also make it clear that these effects are local and disordered on the long-range scale.

ACKNOWLEDGMENTS

The authors thank Prof. W. H. McCarroll and Dr. M. Lobanov for their critical review of the manuscript before its submission. This work was supported by the NSF-Solid State Chemistry Grant DMR 99-07963.

REFERENCES

1. B. Raveau, A. Maignan, C. Marting, and M. Hervieu, *Chem. Mater.* **10,** 2641 (1998).
2. R. C. O'Handley "Modern Magnetic Materials." John Wiley & Sons, Inc., New York, 2001.
3. Y. Moritomo, A. Asamitsu, H. Kuwahara, and Y. Tokura, *Nature* **380,** 141 (1996).
4. S. N. Ruddlesden and P. Popper, *Acta Crystallogr.* **10,** 538 (1957).
5. S. N. Ruddlesden and P. Popper, *Acta Crystallogr.* **11,** 54 (1958).
6. S. Kawasaki, M. Takano, and Y. Takeda, *J. Solid State Chem.* **121,** 174 (1996).
7. A. Maignan, C. Martin, N. Nguyen, and B. Raveau, *Solid State Sci.* **3,** 57 (2001).
8. S. Ghosh and P. Adler, *Solid State Commun.* **116,** 585 (2000).
9. F. Prado and A. Manthiram, *J. Solid State Chem.* **158,** 307 (2001).
10. Y. Bréard, C. Michel, A. Maignan, and B. Raveau, *Solid State Commun.* **118,** 517 (2001).
11. G. M. Veith, I. D. Fawcett, M. Greenblatt, M. Croft, and I. Nowik, *Int. J. Inorg. Mater* **2,** 513 (2000).
12. P. D. Battle, W. R. Branford, A. Mihut, M. J. Rosseinsky, J. Singleton, J. Sloan, L. E. Spring, and J. F. Vente, *Chem. Mater.* **11,** 674 (1999).
13. F. Licci, G. Turilli, and P. Ferro, *J. Magn. Magn. Mater.* **164,** L268 (1996).
14. A. C. Larson and R. B. von Dreele, GSAS–Generalized Crystal Structure Analysis System, Los Alamos National Laboratory Report No. LA-UR-86-748, 1987.
15. S. E. Dann, M. T. Weller, and D. B. Currie, *J. Solid State Chem.* **97,** 179 (1992).
16. R. D. Shannon and C. T. Prewitt, *Acta Crystallogr. B* **25,** 925 (1969).
17. R. D. Shannon, *Acta Crystallogr. A* **32,** 751 (1976).
18. G. M. Veith, M. Greenblatt, M. Croft, K. V. Ramanujachary, J. Hattrick-Simpers, S. E. Lofland and I. Nowik, *Chem. Mater.* (2001), Submitted.
19. S. E. Dann and M. T. Weller, *J. Solid State Chem.* **115,** 499 (1995).
20. M. Takano, J. Kawachi, N. Nakanishi, and Y. Takeda, *J. Solid State Chem.* **39,** 75 (1981).
21. G. Demazeau, B. Buffat, F. Ménil, L. Fournès, M. Pouchard, J. M. Dance, P. Fabritchnyi, and P. Hagenmuller, *Mater. Res. Bull.* **16,** 1465 (1981).
22. I. D. Fawcett, G. M. Veith, M. Greenblatt, M. Croft, and I. Nowik, *J. Solid State Chem.* **155,** 96 (2000).
23. I. D. Fawcett, G. M. Veith, M. Greenblatt, M. Croft, and I. Nowik, *Solid State Sci.* **2,** 821 (2000).
24. M. Z. Cieplak, K. Karpinska, J. Domagala, E. Dynowska, M. Berkowski, A. Malinowski, S. Guha, M. Croft, and P. Lindenfeld, *Appl. Phys. Lett.* **73,** 2823 (1998).
25. G. Liang, Y. Guo, D. Badresingh, W. Xu, Y. Tang, M. Croft, J. Chen, A. Sahiner, and J. T. Markert, *Phys. Rev. B* **51,** 1258 (1995).
26. A. Sahiner, M. Croft, S. Guha, I. Perez, Z. Zhang, M. Greenblatt, P. A. Metcalf, H. Jahns, and G. Liang, *Phys. Rev. B* **51,** 5879 (1995).
27. N. F. Mott and E. A. Davis, Electronic Processes in Non-crystalline Materials Clardenon Press, Oxford, 1979.
28. J. B. Goodenough, *J. Phys. Chem. Solids* **6,** 287 (1958).
29. J. Kanamori, *J. Phys. Chem. Solids* **10,** 87 (1959).
30. T. Kimura, Y. Tomioka, H. Kuwahara, A. Asamitsu, M. Tamura, and Y. Tkura, *Science* **274,** 1698 (1996).
31. T. G. Perring, G. Aeppli, S. M. Hayden, Y. Moritomo, Y. Tokura, J. P. Remeika, and S. W. Cheong, *Physica B* **234–236,** 698 (1997).
32. L. E. Hueso, F. Rivadulla, R. D. Sánchez, D. Caeiro, C. Jardón, C. Vázquez-Vázquez, J. Rivas and M. A. López-Quintela, *J. Magn. Magn. Mater.* **189,** 321 (1998).
33. Y. Takeda, S. Naka, M. Takano, T. Shinjo, T. Takada, and M. Shimada, *Mater. Res. Bull.* **13,** 61 (1978).